Physics in Medicine &
Biology

PAPER

SBL-LCGL: sparse Bayesian learning based on Laplace distribution for robust cone-beam x-ray luminescence computed tomography

To cite this article: Yifan Wang *et al* 2024 *Phys. Med. Biol.* **69** 175020

IOP Publishing Phys. Med. Biol. 69 (2024) 175020 https://doi.org/10.1088/1361-6560/ad7223

Physics in Medicine & Biology

IPEM
Institute of Physics and Engineering in Medicine

CrossMark

RECEIVED
26 June 2024

REVISED
16 August 2024

ACCEPTED FOR PUBLICATION
21 August 2024

PUBLISHED
30 August 2024

PAPER

SBL-LCGL: sparse Bayesian learning based on Laplace distribution for robust cone-beam x-ray luminescence computed tomography

Yifan Wang[1], **Haoyu Wang**[1], **Qiuquan Zhu**[1], **Yi Chen**[1], **Linzhi Su**[1], **Huangjian Yi**[1], **Chengyi Gao**[2] **and Xin Cao**[1,*]

[1] School of Information Science and Technology, Northwest University, Xi'an, Shaanxi 710127, People's Republic of China
[2] Department of Oncology, The First Affiliated Hospital, Xi'an Jiaotong University, Xi'an, Shaanxi 710061, People's Republic of China
[*] Authors to whom any correspondence should be addressed.

E-mail: sulinzhi029@163.com and caoxin918@hotmail.com

Keywords: cone-beam x-ray luminescence computed tomography, SBL-LGCL, sparse Bayesian learning, inverse problems

Abstract

Objective. To address the quality and accuracy issues in the distribution of nanophosphors (NPs) using Cone-beam x-ray luminescence computed tomography (CB-XLCT) by proposing a novel reconstruction strategy. *Approach*. This paper introduces a sparse Bayesian learning reconstruction method termed SBL-LCGL, which is grounded in the Lipschitz continuous gradient condition and the Laplace prior to overcome the ill-posed inverse problem inherent in CB-XLCT. *Main results*. The SBL-LCGL method has demonstrated its effectiveness in capturing the sparse features of NPs and mitigating the computational complexity associated with matrix inversion. Both numerical simulation and *in vivo* experiments confirm that the method yields satisfactory imaging results regarding the position and shape of the targets. *Significance*. The advancements presented in this work are expected to enhance the clinical applicability of CB-XLCT, contributing to its broader adoption in medical imaging and diagnostics.

1. Introduction

X-ray luminescence computed tomography (XLCT) is one hybrid imaging modality, which combines the high molecular sensitivity of optical imaging and the excellent spatial resolution of x-ray imaging (Zhang *et al* 2019). As a branch of optical molecular imaging technology, XLCT has received attention in the field of biomedical research because it can provide qualitative and quantitative information at the cellular and molecular levels (Qin *et al* 2011). In XLCT, nanophosphors (NPs) within a biological organism are irradiated by externally applied x-ray beams, leading to the generation of near-infrared (NIR) light. This light can propagate through the tissue and be measured by the charge coupled device (CCD) (Chen *et al* 2023). XLCT offers superior image quality over x-ray imaging modalities and has the ability to provide structural information inside the object (Ahmad *et al* 2014). Compared with other optical molecular tomography modalities, XLCT has its unique advantages. For example, compared with fluorescence molecular tomography, since the fluorescent probe can only be excited and luminescent by x-rays, XLCT can effectively reduce the interference of autofluorescence (Mishra and Kappiyoor 2014); compared with bioluminescence tomography, XLCT effectively solves the limitation of low photon count by adopting a selective excitation scheme under the standard radiation dose (Pratx *et al* 2010). So far, the XLCT technology has been successfully applied in tumor imaging and treatment: Oh *et al* used XLCT for angiography and bimodal image-guided lymph node imaging (2011). Kinsella *et al* applied XLCT to breast cancer tumor imaging (2011). These studies have effectively promoted the clinical transformation of XLCT. XLCT system has three main categories: pencil-beam XLCT, cone-beam XLCT, and narrow-beam XLCT (Chen *et al* 2015). Compared with the others, Cone-beam x-ray luminescence computed tomography (CB-XLCT) utilizes the cone-beam geometric shape to cover the entire imaging object. This simplifies the scanning process and is more conducive to rapid biomedical imaging (Liu *et al* 2018).

Accurate reconstruction in XLCT is contingent upon two pivotal factors: a precise photon transmission model and an adept reconstruction algorithm. Given the inherent low absorption and high scattering of light, XLCT is fraught with the challenges of a severely ill-posed inverse problem, which can significantly degrade reconstruction quality (Liu *et al* 2021). To address this, various strategies have been explored to refine the reconstruction process. Some researchers have integrated structural information and PSR into their reconstruction algorithms to improve the specificity and accuracy of the reconstruction. This approach leverages prior knowledge about the sample's structure, which can guide the reconstruction process and reduce ambiguity (Hu *et al* 2012, Ding *et al* 2014, Guo *et al* 2018). Regularization has emerged as a dominant strategy to mitigate the ill-posedness of XLCT. Guo *et al* proposed a non-convex sparse regularization algorithm, which enhances the algorithm's capacity to resolve multiple sources by specifically targeting sparse solutions (2017). In addition, the L_1-norm, acting as a convex surrogate for the L_0-norm, is instrumental in promoting sparsity in the solution space (Zhang *et al* 2011). Based on the L_1-norm, Gao *et al* introduced the restarted primal-dual Newton conjugate gradient method, which employs a restarted strategy to counteract the ill-posedness of CB-XLCT more effectively (2020). In an effort to harness the strengths of different regularization techniques, hybrid methods have been developed. Liu *et al* combined L_1 and total-variation regularization, which not only improves image resolution but also introduces a measure of smoothness to the reconstruction, thereby enhancing the visual quality of the images (Liu *et al* 2019). Zhao *et al* combined L_1 and L_2 regularization in proposing the Elastic Net-L_1L_2 method to enhance the sparsity and suppress the smoothness of specific solutions (2021). While regularization methods have made strides in enhancing reconstruction quality, they often grapple with the challenge of parameter determination. Improper parameter selection can severely impact the fidelity of the reconstruction results. The dictionary learning-based algorithms are well-suited for tackling inverse problem, however, they face a significant challenge in the substantial computational resources they require. Moreover, the optimization and tuning of hyperparameters within these algorithms are notably intricate processes, often demanding a high level of expertise and extensive computational effort.

Different from the above methods, some algorithms based on the Bayesian framework are less difficult in parameter selection and are well suited to solving inverse problems. The Bayesian method based on the Gaussian Markov random field achieves reconstruction with high image contrast and low localization error (Zhang *et al* 2018). Yin *et al* gave a Gaussian prior information on the distribution of light sources to improve the quality of reconstruction (2021). In comparison, the Laplace prior is more suitable for the sparsity of the NPs distribution (Zhang *et al* 2017). Wu *et al* used the weighted Laplace prior for lung respiratory monitoring with Electrical Impedance Tomography (2023). The Laplace prior and some deformations are widely used to solve sparse data (Bai and Sun 2023). Bayesian learning algorithms, on the other hand, have demonstrated an aptitude for integrating sparsity more effectively, offering a promising avenue for future research.

In the sparse Bayesian learning (SBL) framework, the major challenge lies in the excessively high computational complexity (Fang *et al* 2016). To overcome the drawback, the E-step in SBL is replaced by Vector Approximate Message Passing with the variance auto-tuning, thus reducing the number of iterations (Ruan *et al* 2023). Under certain conditions, the likelihood function is replaced by a surrogate function to avoid the matrix inversion process (Zhang and Dai 2022). The space alternating approach can also be employed to reduce computational complexity (Bai *et al* 2022).

In this paper, we introduce an innovative SBL approach for the reconstruction of CB-XLCT, known as SBL-LCGL, which is designed to tackle the issue of high computational complexity while achieving satisfactory reconstruction quality. Our method breaks through the limitations of traditional approaches by incorporating a Laplace prior to capture the sparse distribution characteristic of the light source relative to the entire imaging object. Although the Laplace distribution is not a conjugate prior to the likelihood function's prior information, typically assumed to be Gaussian distribution (Glaubitz 2023), we have ingeniously addressed this non-conjugate issue, significantly reducing the computational burden. Within the SBL framework, the primary challenge we faced was the high computational complexity due to matrix inversion operations. By replacing the quadratic term in the light source distribution likelihood function, we have not only demonstrated a reduction in complexity but also, through the introduction of a Taylor series expansion, transformed the originally non-convex problem into a convex optimization problem, which simplifies the process of solving for hyperparameters (Sun *et al* 2017). Ultimately, the experimental results have proven the significant effectiveness of our proposed method in improving the quality of reconstruction, as well as highlighting its superior performance in practical applications.

The remaining structure of the article is described as follows: In section 2, we introduced the photon propagation model of CB-XLCT and the SBL-LCGL method. In section 3, numerical simulations and in vivo experiment were conducted to demonstrate the effectiveness of the proposed approach. Section 4 provides a discussion and summary of this paper.

2. Methods

During the CB-XLCT imaging process, x-ray emitted from cone-beam incoherent x-ray sources traverse through the tissues of biological organisms, and the NPs distributed in the imaging object can emit visible or NIR light. The x-ray intensity at position r $X(r)$ and the energy density of these lights $S(r)$ can be calculated using the following formula (Liu *et al* 2015):

$$\begin{aligned} X(r) &= X(r_0)\exp\left\{-\int_{r_0}^{r}\mu_t(\tau)\,\mathrm{d}\tau\right\} \\ S(r) &= \rho X(r)\,n_c(r) \end{aligned} \tag{1}$$

where $X(r_0)$ is the x-ray intensity at the initial position r_0, $\mu_t(\tau)$ denotes the x-ray attenuation coefficient at position τ. ρ represents the light yield of nanoparticles, and $n_c(r)$ is the NPs concentration at position r. Typically, the Radiative Transfer Equation (RTE) model (Zhang *et al* 2011) is used to characterize the propagation of light. However, due to the high complexity in solving the RTE model and the characteristics of high light scattering and low absorption in optical processes, the following steady-state diffusion equation model with Robin-type boundary conditions is adopted for modeling (Klose *et al* 2010).

$$\begin{aligned} -\nabla\left[D(r)\nabla\Phi(r)\right] + \mu_a(r)\Phi(r) &= S(r),\ r\in\Omega \\ \times\Phi(r) + 2\varepsilon D(r)\left[\nu(r)\cdot\nabla\Phi(r)\right] &= 0,\ r\in\partial\Omega \end{aligned} \tag{2}$$

where Ω is the domain of the imaged object and $\partial\Omega$ is the boundary of Ω. The diffusion coefficient, denoted as $D(r)$, can be calculated using $D(r) = 1/3\left(\mu_a(r) + \mu'{}_s(r)\right)$, where $\mu_a(r)$ is the optical absorption coefficient and $\mu_s'(r)$ is the reduced scattering coefficient at the position r. ε and $\nu(r)$ are the mismatch factor and the outward unit normal vector on the boundary $\partial\Omega$, respectively. $\Phi(r)$ represents the photon fluence rate at position r.

Using the finite element method on the aforementioned photon propagation model (Wang *et al* 2006), a linear relationship can be obtained between the light source vector on the object surface and the NPs density to be reconstructed:

$$K\Phi = Fx \tag{3}$$

with

$$\begin{aligned} K_{ij} &= \int_{\Omega}\left(D(r)\nabla\psi_i(r)\nabla\psi_j(r) + \mu_a\nabla\psi_i(r)\nabla\psi_j(r)\right)\mathrm{d}r + \frac{1}{2\varepsilon}\int_{\partial\Omega}\psi_i(r)\nabla\psi_j(r))\mathrm{d}r \\ F_{ij} &= \int_{\Omega}\Phi(r)\psi_i(r)\psi_j(r)\,\mathrm{d}r \end{aligned} \tag{4}$$

where x is the $N\times 1$ NPs density to be reconstructed. K_{ij} and F_{ij} are the elements of matrix K and F, respectively.

ψ_i and ψ_j denote the corresponding elements of the function. Since the K is positive definite, the linear relationship can be rewritten as

$$\Phi = Ax. \tag{5}$$

Taking into account the biases present in data measurement and processing (Gao *et al* 2018), the final linear relationship is derived as follows:

$$\Phi = Ax + \eta \tag{6}$$

where A is the system weight matrix with size of $M\times N$. The known vector Φ is the light source on the object surface and η represents the sum of measurement errors and noise.

2.1. SBL-LCGL model

In XLCT, the NP in biological tissues is usually unevenly distributed, which means that the image is somewhat sparse. Sparse Bayesian frameworks can effectively take advantage of this sparsity to reconstruct an image by learning a small number of non-zero elements. At the same time, the sparse Bayesian framework allows the prior knowledge to be integrated into the model, and the prior knowledge of the biological organization structure can be used to guide the reconstruction process.

In the sparse Bayesian framework, all unknown parameters and hyperparameters are treated as stochastic variables with specified probability distributions based on the characteristics of the data (Bai 2023). The entire process of sparse Bayesian inference is based on formula (4). The Bayesian theorem allows us to combine prior information with newly observed data, leading to more accurate maximum a posteriori estimation (Wu *et al* 2023).

$$p\left(x|\Phi\right) = \frac{p\left(\Phi|x\right)p\left(x\right)}{p\left(\Phi\right)} \tag{7}$$

where $p\left(x\right)$ represents the prior probability, typically specified based on the characteristics of the data and $p\left(\Phi|x\right)$ is the likelihood function of observing the data and the sum of measurement errors and noise. $p\left(x|\Phi\right)$ denotes the posterior probability of the unknown parameters given the observed data. The denominator $p\left(\Phi\right)$ serves as the marginal likelihood.

Due to the fact that the Laplace distribution is more suitable for sparse data (Tang *et al* 2022), such as the NPs distribution that needs to be reconstructed, we adopt the Laplace distribution as prior information. However, the Laplace distribution is not conjugate to the Gaussian distribution assumed for the likelihood function mentioned later, and a tractable Bayesian inference is not allowed, thereby increasing computational complexity. To address this challenge, a hierarchical model is employed here and assumes the vectors in x are independently and identically distributed.

$$p\left(x\right) = \prod_{i=1}^{N} p\left(x_i\right) = \prod_{i=1}^{N}\int p\left(x_i|\omega_i\right)p\left(\omega_i\right)\mathrm{d}\omega_i \tag{8}$$

where ω_i is a hyperparameter and $p\left(\omega_i\right)$ is its distribution and we define the hyperparameter set $\omega = \left(\omega_1, \omega_2, \ldots \omega_N\right)$.

Specifically, to ensure that $p\left(x\right)$ follows a Laplace distribution, it is common to model $p\left(x_i|\omega_i\right)$ as a Gaussian distribution with zero mean and variance ω_i, that is $p\left(x_i|\omega_i\right) \sim \mathcal{N}\left(x_i|0, \omega_i\right)$. The distribution $p\left(\omega_i\right)$ is typically assumed to follow a gamma distribution, that is $p\left(\omega_i\right) \sim \Gamma\left(\omega_i|1, \alpha/2\right)$. The inference proceeds as follows:

$$p\left(x\right) = \prod_{i=1}^{N}\int \frac{1}{\sqrt{2\pi\omega_i}}\exp\left\{-\frac{x_i^2}{2\omega_i}\right\}\cdot\frac{\alpha}{2}\exp\left\{-\frac{\alpha\omega_i}{2}\right\}\mathrm{d}\omega_i = \frac{\alpha^{\frac{N}{2}}}{2^N}\exp\left(-\alpha^{\frac{1}{2}}\sum_i |x_i|\right). \tag{9}$$

Then the sum of measurement errors and noise η is assumed to be the Gaussian distribution with zero mean and variance equal to β^{-1}, that is $p\left(\eta\right) \sim \mathcal{N}\left(0, \beta^{-1}\right)$. Assuming the hyperprior for β follows a gamma distribution: $p\left(\beta\right) \sim \Gamma\left(\beta|a_\beta,\ b_\beta\right)$. Based on equation (6), the likelihood function of observed data follows the following distribution:

$$p\left(\Phi|x, \beta\right) = \left(2\pi\beta^{-1}\right)^{-\frac{1}{2}}\exp\left\{-\frac{\|\Phi - \mathrm{A}x\|^2}{2\beta^{-1}}\right\}. \tag{10}$$

It is evident that $p\left(\Phi|x, \beta\right)$ follows a Gaussian distribution, that is $p\left(\Phi|x, \beta\right) \sim \mathcal{N}\left(\mathrm{A}x, \beta^{-1}\right)$. However, a challenge arises as the resulting update formulas involve the process of matrix inversion, which can be computationally disadvantageous in terms of speed (Shutin *et al* 2011). Inspired by (Nesterov 2013), the Lipschitz continuous gradient condition is incorporated into the sparse Bayesian framework.

The Lipschitz continuous gradient refers to a condition where the gradient of a function remains Lipschitz continuous throughout its entire domain and there exists a Lipschitz constant L, for any $c, d \in \mathrm{R}^n$ the norm of the gradient of the function satisfies the following inequality:

$$||\nabla f(c) - \nabla f(d)|| \leqslant L\,\|c - d\|,\ \ \forall c, d \tag{11}$$

where $\nabla f(c)$ represents the gradient of the function f at point c and $\|\cdot\|$ denotes the norm of a vector. In the quadratic term $f(x) = \|\Phi - \mathrm{A}x\|^2$, which satisfies the Lipschitz continuous gradient condition, the following inequality is adopted as a replacement function.

$$f(x) \leq f(z) + \nabla f(z)^T (x - z) + \frac{L}{2}\|x - z\|^2, \ \forall x, z. \tag{12}$$

For any $x, z \in \mathbb{R}^n$, substituting the function f and simplifying, we obtain:

$$\|\Phi - Ax\|^2 \leq \|\Phi - Az\|^2 + 2(x - z)^T A^T (Az - \Phi) + \frac{L}{2}\|x - z\|^2. \tag{13}$$

It is noted that the equation holds if and only if $x = z$, thereby let $Z(x, z) = \|\Phi - Az\|^2 + 2(x - z)^T A^T (Az - \Phi) + \frac{L}{2}\|x - z\|^2$ and the likelihood function can be represented as:

$$p(\Phi|x, \beta) = \max_z \bar{p}(\Phi|x, \beta; z) = \max_z \left(2\pi\beta^{-1}\right)^{-\frac{1}{2}} \exp\left\{-\frac{Z(x, z)}{2\beta^{-1}}\right\}. \tag{14}$$

Due to the difficulty in maximizing the operation for $\bar{p}(\Phi|x, \beta; z)$, a suggested approach is to set a fixed value for z, that is z_p. Then we can get the strict lower bound for $p(\Phi|x, \beta)$, and the posterior probability can then be solved using the following equation:

$$p(x|\Phi, \beta, \omega) \approx \frac{\bar{p}(\Phi|x, \beta; z_p)\, p(x|\omega)}{\int \bar{p}(\Phi|x, \beta; z_p)\, p(x|\omega)\, \mathrm{d}x} = (2\pi\Sigma_x)^{-\frac{1}{2}} \exp\left\{-\frac{(x - \mu_x)^2}{2\Sigma_x}\right\} \tag{15}$$

with

$$\begin{aligned} \Sigma_x &= \frac{1}{\Omega^{-1} + \frac{L}{2}\beta}, \ \Omega = \mathrm{diag}(\omega) \\ \mu_x &= \frac{\beta\left(\frac{L}{2}z_p - A^T A z_p + A^T \Phi\right)}{\Omega^{-1} + \frac{L}{2}\beta}. \end{aligned} \tag{16}$$

According to sparse Bayesian inference, the value of the NPs distribution in each iteration should be chosen to maximize the posterior probability.

$$x_{\mathrm{iter}} = \mu_x. \tag{17}$$

Subsequently, the Expectation-Maximization algorithm can be used to determine the hyperparameters β, ω, z by maximizing the probability density function excluding x. Starting with $p(\Phi, x, \beta, \omega)$:

$$p(\Phi, \beta, \omega) = \int \max_z \bar{p}(\Phi|x, \beta; z)\, p(x|\omega)\, p(\beta)\, p(\omega)\, \mathrm{d}x. \tag{18}$$

For the sake of facilitating subsequent calculations, the maximization operation is positioned after the integration operation. Through the derivation, when $A^T A = L/2$, the difference of the resulting substitution is zero. The solution for hyperparameters is accomplished by the following expression:

$$(\beta, \omega, z) = \arg\max_{\beta, \omega, z} \int \bar{p}(\Phi|x, \beta; z)\, p(x|\omega)\, p(\beta)\, p(\omega)\, \mathrm{d}x. \tag{19}$$

Continuing with the treatment of the integration operation, it can be observed that:

$$\int \bar{p}(\Phi|x, \beta; z)\, p(x|\omega)\, p(\beta)\, p(\omega)\, \mathrm{d}x = p(\beta)\, p(\omega) \left(\frac{1}{2\pi\beta^{-1}}\right)^{\frac{1}{2}} \left|\Omega\Sigma_x^{-1}\right|^{-\frac{1}{2}} \exp\left\{-\frac{1}{2}H(\beta, \omega, z)\right\} \tag{20}$$

with

$$H(\beta, \omega, z) = \beta\left(\|\Phi - Az\|^2 - 2z^T A^T (Az - \Phi) + \frac{L}{2}z^T z\right) - {\mu_x}^T \Sigma_x^{-1} \mu_x. \tag{21}$$

By substituting Σ_x and μ_x and applying $-2\ln(\cdot)$ operation to the above expression, the cost function is obtained:

$$C(\beta, \omega, z, x) = C_{(\beta, \omega_i)} + \sum_{i=1}^{N} \alpha\omega_i - 2\ln\left(\frac{\alpha}{2}\right) - C_{\mathrm{const}}\ln\beta^{-1} + \beta\left(Z(x, z) + 2b_\beta\right) + \sum_{i=1}^{N} \frac{x_i^2}{\omega_i} \tag{22}$$

Algorithm 1. SBL-LCGL method for CB-XLCT Reconstruction.

```
Input: The system matrix $A$ and the measured surface photon $\Phi$
Initialization: The hyperparameters: $\beta^{(0)}, \omega^{(0)}, z^{(0)}$ and the constants: $a_\beta, b_\beta, \alpha$, err,iter$_{\max}$
Step1: Compute fixed values:$A^TA,\ A^T\Phi$
Step2:
While iter$_{\text{current}}\langle$iter$_{\max}$or$\left\|x_{\text{iter}}^{(i+1)} - x_{\text{iter}}^{(i)}\right\|_2\rangle$err do
    (1): Maximize the posterior probability stage:
    Update the mean of the posterior probability and set $x_{\text{iter}}^{(i+1)}$ equal to that value, according to the equation (17).
    (2): Minimize the loss function stage:
    Update the values of hyperparameters to minimize the loss function, according to the equation (24).
    (3): $\text{iter}_{\text{current}} = \text{iter}_{\text{current}} + 1$
End while
Output: $x = x_{\text{iter}}^{(i+1)}$
```

where $C_{\text{const}} = N + 2 - M - 2a_\beta, C_{(\beta,\omega_i)} = \sum_{i=1}^{N} \ln\left(\beta^{-1} + \frac{L}{2}\omega_i\right)$.

However, the cost function is not convex and one may encounter local optima. To address this issue, it is advisable to transform it into a convex function and then seek the minimum value. Specifically, for the fourth term in the cost function, assuming $0 < a_\beta < (N - M + 2)/2$, this term is convex. The non-convexity of the cost function primarily arises from the first term $C_{(\beta,\omega_i)}$. Therefore, the commonly employed first-order Taylor expansion, widely used in fields such as signal processing, communications, and machine learning, is utilized for approximation.

The final approximation of the cost function is denoted by C_{appr} in the following expression.

$$C_{\text{appr}}(\beta,\omega,z,x) = g(\beta,\omega) + J(\beta,\omega,z,x) \tag{23}$$

where $J(\beta,\omega,z,x) = \sum_{i=1}^{N} \alpha\omega_i - 2\ln\left(\frac{\alpha}{2}\right) - C_{\text{const}}\ln\beta^{-1} + \beta\left(Z(x,z) + 2b_\beta\right) + \sum_{i=1}^{N} \frac{x_i^2}{\omega_i}$.

Due to the separability of the cost function and the sparsity nature of the reconstruction problem, the Coordinate Descent algorithm is employed to iteratively update the hyperparameters until convergence (Parikh 2014).

$$\begin{aligned}
x_{\text{iter}}^{(i+1)} &= \frac{\left(\frac{L}{2}z^{(i)} - A^TAz^{(i)} + A^T\Phi\right)}{\left(\frac{1}{\Omega^{(i)}\beta^{(i)}} + \frac{L}{2}\right)} \\
z^{(i+1)} &= x_{\text{iter}}^{(i+1)} \\
\beta^{(i+1)} &= \frac{2\sum_{i=1}^{N}\left(\beta^{-1^{(i)}} + \frac{L}{2}\omega_i{}^{(i)}\right)^{-1}}{C_{\text{const}} + \sqrt{C_{\text{const}}{}^2 + 4\sum_{i=1}^{N}\left(\beta^{-1^{(i)}} + \frac{L}{2}\omega_i{}^{(i)}\right)^{-1}\left(\left\|\Phi - Az^{(i+1)}\right\|^2 + 2b_\beta\right)}} \\
\omega^{(i+1)} &= \left|x_{\text{iter}}^{(i+1)}\right|\left(\sqrt{\alpha + \frac{\frac{L}{2}}{\beta^{-1^{(i)}} + \frac{L}{2}\omega^{(i)}}}\right)^{-1}
\end{aligned} \tag{24}$$

3. Experiments and results

In this section, the performance of SBL-LCGL is evaluated through a series of numerical simulations and in vivo experiment. Specifically, SBL-LCGL is compared with three existing algorithms: Fast-Laplace, the fast iterative shrinkage thresholding algorithm (FISTA) and the incomplete variables truncated conjugate gradient (IVTCG), focusing primarily on four aspects: positioning accuracy, shape recovery, robustness, and in vivo practicability. All experiments and programs are performed on a desktop computer equipped with Inter(R) Core$^{\text{TM}}$i5-13490F CPU(2.50 GHz) and 32GB RAM.

3.1. Evaluation metrics

To comprehensively evaluate the performance of the proposed method in CB-XLCT reconstruction, particularly in terms of reconstruction quality and accuracy, five primary quantitative evaluation metrics are employed: location error (LE), dice similarity coefficient (DICE), mean squared error (MSE), structural similarity (SSIM), and volume ratio (VR).

The LE is an index to evaluate spatial positioning accuracy by calculating the Euclidean distance between the central coordinates of the reconstructed region $L_r(x_r, y_r, z_r)$ and the actual regional central coordinates $L_t(x_t, y_t, z_t)$. The definition is as follows:

$$LE = \|L_r - L_t\|_2. \tag{25}$$

The DICE offers a quantitative measure to assess spatial SSIM between the reconstructed target S_r and the actual target S_t. The DICE value ranges between 0 and 1, with a value closer to 1 indicating a higher degree of similarity between the reconstructed and actual targets, consequently the better shape recovery. The calculation formula for DICE is as follows:

$$\mathrm{DICE} = 2\frac{|S_r \cap S_t|}{|S_r| + |S_t|}. \tag{26}$$

The VR is a metrics used to assess the shape and size between the true light source tetrahedron V_{true} and the reconstructed light source tetrahedron V_{recon} :

$$\mathrm{VR} = \frac{V_{\mathrm{true}}}{V_{\mathrm{recon}}}. \tag{27}$$

The VR close to 1 indicates that the volume of the reconstructed light source is very close to that of the true light source.

The MSE is widely used to measure the gap between predicted values and actual values and it provides a quantitative measure of the model's prediction accuracy by calculating the average of the sum of squared errors. The definition of MSE is as follows:

$$\mathrm{MSE} = \frac{1}{N}(x - \hat{x})^T (x - \hat{x}) \tag{28}$$

where x represents the distribution of reconstructed NPs and $\hat{x}$ represents the distribution of actual NPs. And the closer the value of MSE is to zero, the higher the reconstruction fidelity.

The definition of SSIM is as follows:

$$\mathrm{SSIM}(R, A) = \frac{(2\mu_R\mu_A + c_1)(2\sigma_{RA} + c_2)}{(\mu_R^2 + \mu_A^2 + c_1)(\sigma_R^2 + \sigma_A^2 + c_2)} \tag{29}$$

where μ_R is the average value of the reconstructed light source intensity, μ_A is the average value of the actual light source intensity, σ_R is the standard deviation of the reconstructed light source intensity, σ_A is the standard deviation of the actual light source intensity, σ_{RA} is the covariance between the actual light source and the reconstructed light source intensity, and the two parameters c_1 and c_2 represent constants related to the dynamic range of the light source values.

3.2. Numerical simulations

To evaluate the performance of the proposed method, a non-uniform cylindrical phantom with a height of 30 mm and a radius of 10 mm was employed as the model and simulated five major organs: heart, bone, liver, lungs, and muscle, as shown in figure 1(A). The optical properties of these tissues are detailed in table 1 (Jacques 2013). A small spherical radiative source with a diameter of 1 mm is embedded in the model to simulate the location of a tumor. To ensure effective photon penetration, 650 nm was selected as the wavelength for the photons. In the simulation experiments, the cylindrical phantom was rotated 360° with light emission images collected every 90° for reconstruction, resulting in a total of four different projection angles. The x-ray attenuation coefficient was set at 0.0535 mm^{-1}, and the operational parameters of the cone-beam x-ray source were set at 48°kV and 0.8 mA. During the reconstruction process, the COMSOL Multiphysics 5.6 (COMSOL, Inc., Burlington, Massachusetts) software (Parvitte *et al* 2013) was used to transform the model into a unified tetrahedral mesh consisting of 4,626 nodes and 25 840 tetrahedral elements, as shown in figure 1(B). Using the Molecular Optical Simulation Environment (MOSE, Version 2.3) software (Ren *et al* 2013), the Monte Carlo method was implemented to successfully obtain forward simulation results, which are displayed in figure 1(C).

3.2.1. Reconstruction result of the single light source simulation

In the single light source reconstruction experiment, a sphere was implanted to simulate the actual light source, with its central coordinates at (−6, −4, 6) mm. The results of the single light source reconstruction are presented in figure 2, where the first row exhibits the 3D views reconstructed by the four methods, and the second row shows the sectional insights at $z = 6.00$ mm. The black circle in these sections indicates the actual location of the light source. Table 2 lists the quantitative results of the single light source

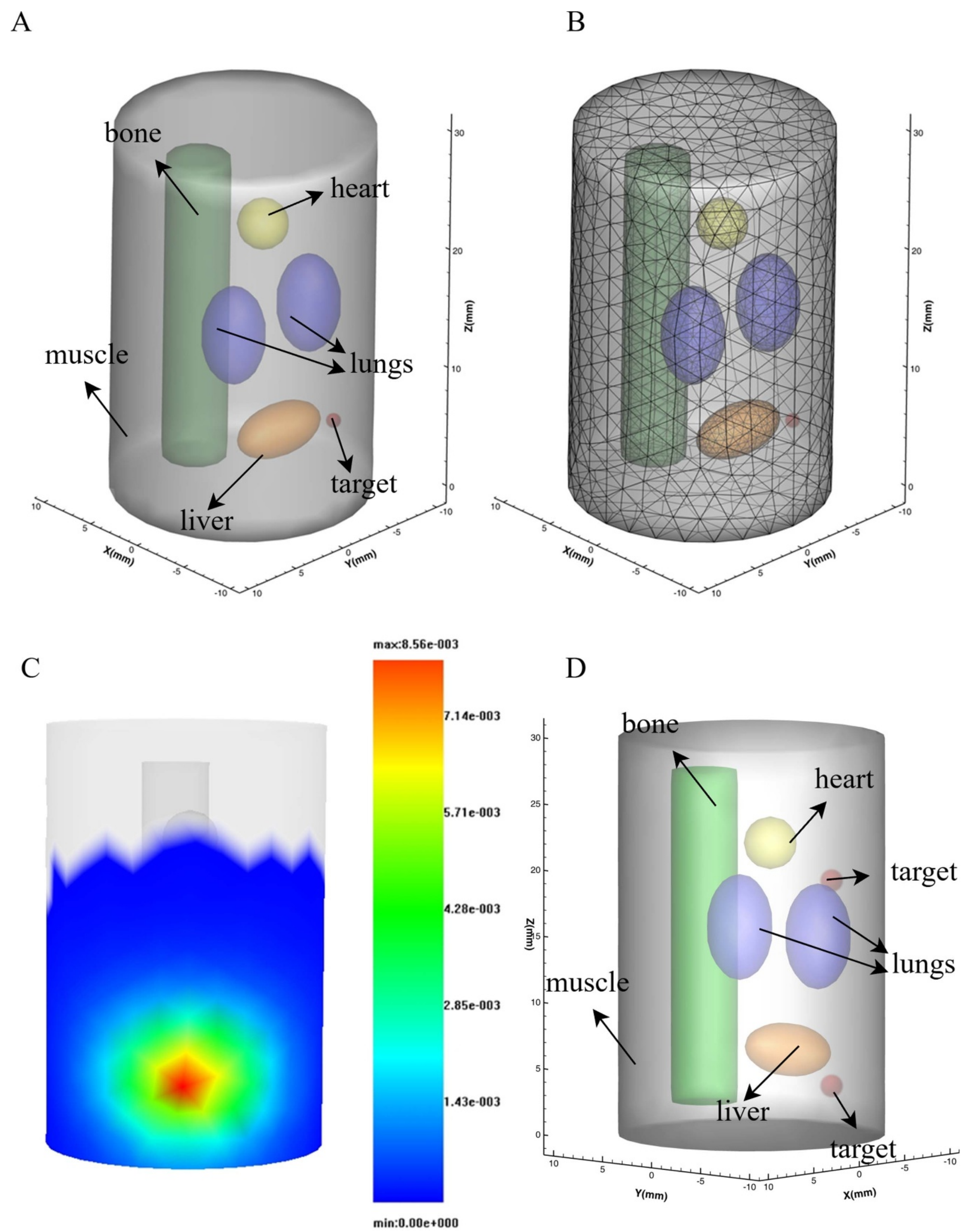

Figure 1. (A) The 3D view of the main organs of the single light source cylinder model. (B) Finite element tetrahedral mesh obtained after discretizing the model. (C) Forward simulation result using MOSE software. (D) The 3D view of the main organs of the dual light source cylinder model.

Table 1. Optical properties of tissues in the heterogeneous cylindrical phantom at 650 nm.

Tissues	$\mu_{\alpha x}\left(\mathrm{mm}^{-1}\right)$	$\mu'_{sx}\left(\mathrm{mm}^{-1}\right)$	$\mu_{am}\left(\mathrm{mm}^{-1}\right)$	$\mu_{sm}\left(\mathrm{mm}^{-1}\right)$	g
Heart	0.0504	0.9437	0.0331	0.8203	0.90
Bone	0.0521	2.4415	0.0326	2.114	0.93
Liver	0.3016	0.6676	0.1921	0.6023	0.93
Lungs	0.1681	2.1569	0.1045	2.0477	0.93
Muscle	0.0745	0.4115	0.0474	0.3122	0.97

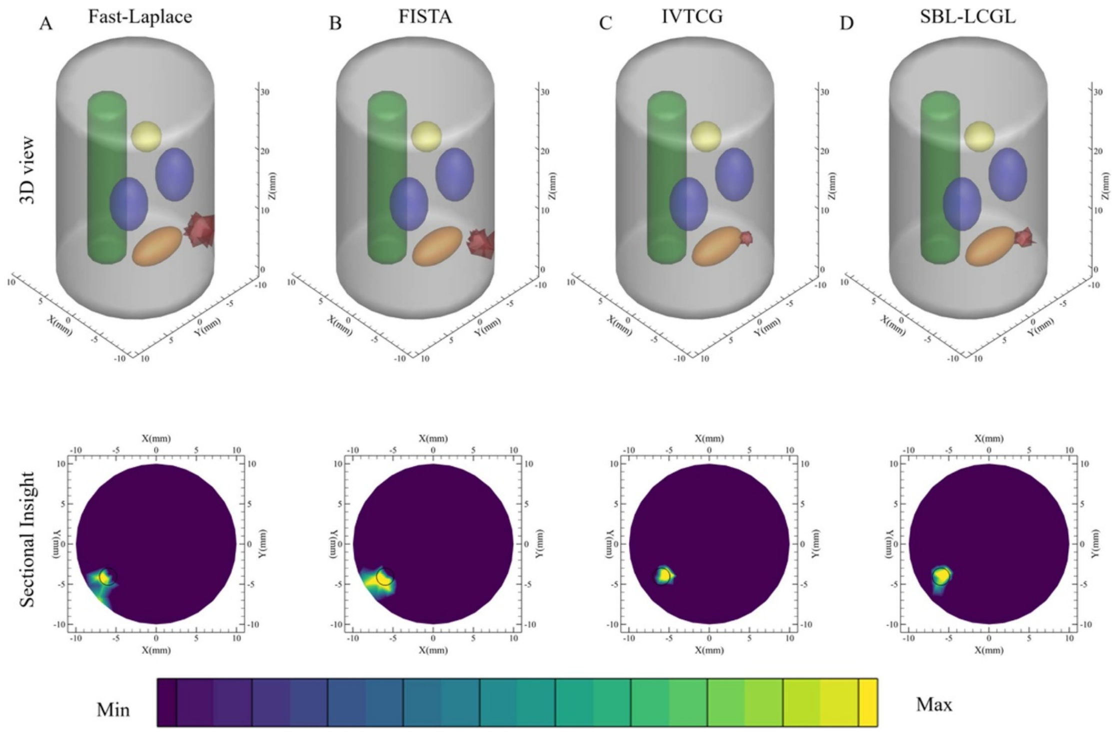

Figure 2. The 3D view of the reconstruction results from four methods. The respective sectional insights at $z = 6.00$ mm.

Table 2. Quantitative results in single light source simulation reconstruction.

Method	True center position	Reconstructed center position	LE(mm)	DICE	MSE	SSIM	VR
Fast-Laplace	(−6.00, −4.00, 6.00)	(−6.49, −4.53, 7.36)	1.55	0.18	0.00562	0.792	0.31
FISTA	(−6.00, −4.00, 6.00)	(−6.41, −4.51, 5.62)	0.76	0.31	0.00475	0.833	0.29
IVTCG	(−6.00, −4.00, 6.00)	(−5.30, −3.78, 5.81)	0.75	0.62	0.00259	0.859	1.61
SBL-LCGL	(−6.00, −4.00, 6.00)	(−5.64, −3.84, 6.04)	0.38	0.75	0.00172	0.906	1.05

reconstruction. The results indicate that the SBL-LCGL method achieves a smaller LE compared to the Fast-Laplace, FISTA, and IVTCG methods, suggesting that the reconstructed coordinates are closer to the true light source coordinates. Furthermore, the SBL-LCGL method yields a higher DICE coefficient, reaching 0.75, which means a high degree of overlap between the reconstructed and actual light sources. Additionally, the results indicate that the method we proposed obtained the smallest MSE and the SSIM closest to 1, which proves that our method has high prediction accuracy. The VR coefficient is closer to 1, indicating that the shape and size of the reconstruction is recovered more accurately. Collectively, these results validate the effectiveness of the proposed method.

3.2.2. Reconstruction result of the dual light source simulation

In the dual light source experiment, we placed two small spheres to simulate the real light source, and the central coordinates were (−5.00, −3.00, 3.00) mm and (−5.00, −3.00, 19.00) mm, respectively. Figure 3 shows the reconstruction results of the four methods. The first row is the 3D view and the second row is the cross section at $y = -3.00$ mm. Table 3 gives a quantitative analysis of the reconstruction results. The proposed method has the smallest LE coefficient and outperforms other methods in both DICE coefficient, MSE coefficient, SSIM coefficient and VR coefficient. This confirms that this method has good light source positioning capabilities and excellent structural recovery capabilities.

3.2.3. Anti-noise experiment

To test the robustness of the SBL-LCGL method to noise, we introduced different proportions of Gaussian noise to the measurement data based on the original single-light source simulation reconstruction experiment. These proportions are 5%, 10%, 15%, 20%, and 25% respectively. According to the results shown in figure 4, even as the proportion of Gaussian noise increases, the reconstruction performance of the SBL-LCGL method does not deteriorate, but improves in some cases. This experimental result fully proves that this method exhibits excellent robustness in the face of data noise.

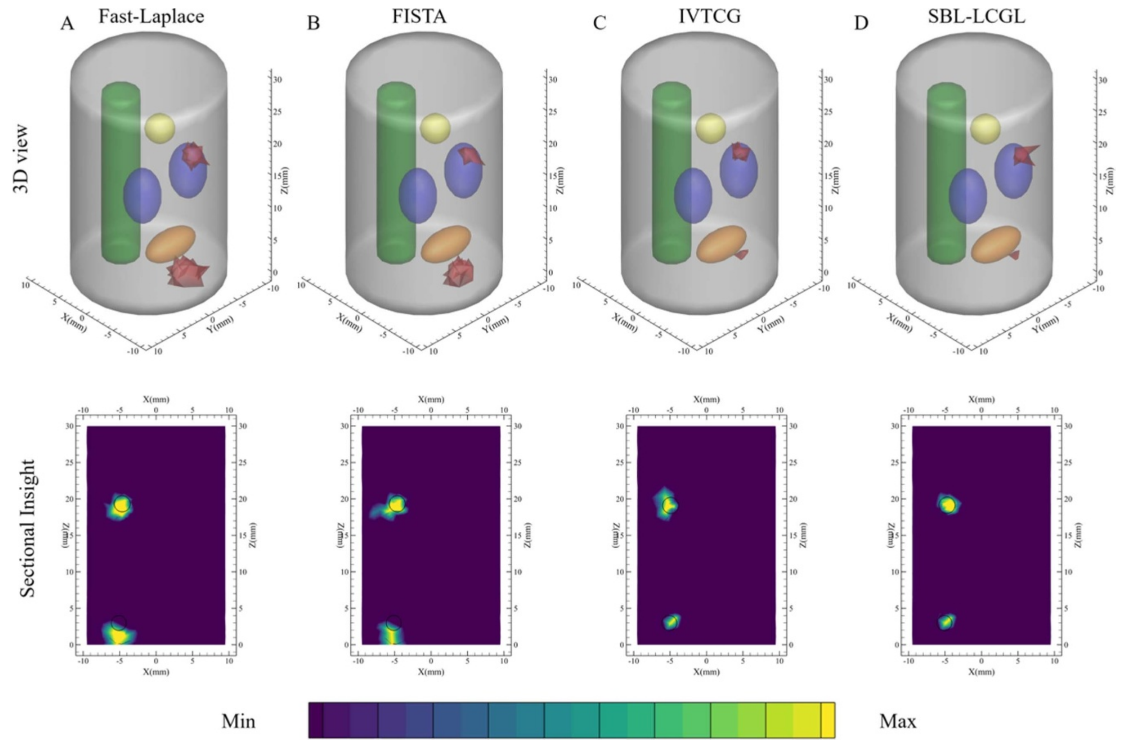

Figure 3. The 3D view of the reconstruction results for dual light sources. The respective sectional insights at $y = -3.00$ mm.

Table 3. Quantitative results in dual light source simulation reconstruction.

Method	True center position	Reconstructed center position	LE(mm)	DICE	MSE	SSIM	VR
Fast-Laplace	(−5.00, −3.00, 3.00)	(−4.87, −1.84, 1.54)	1.86	0.16	0.00689	0.782	0.22
	(−5.00, −3.00, 19.00)	(−4.30, −3.40, 18.63)	0.88	0.11	0.00766	0.815	0.58
FISTA	(−5.00, −3.00, 3.00)	(−4.75, −2.71, 3.36)	0.52	0.50	0.00436	0.832	0.42
	(−5.00, −3.00, 19.00)	(−4.51, −3.35, 18.87)	0.61	0.24	0.00561	0.816	0.79
IVTCG	(−5.00, −3.00, 3.00)	(−4.65, −2.99, 3.27)	0.46	0.66	0.00243	0.853	1.21
	(−5.00, −3.00, 19.00)	(−4.34, −2.98, 19.09)	0.66	0.53	0.00339	0.841	1.18
SBL-LCGL	(−5.00, −3.00, 3.00)	(−4.85, −2.73, 3.22)	0.37	0.85	0.00153	0.883	1.25
	(−5.00, −3.00, 19.00)	(−5.42, −3.32, 19.05)	0.53	0.71	0.00181	0.867	1.09

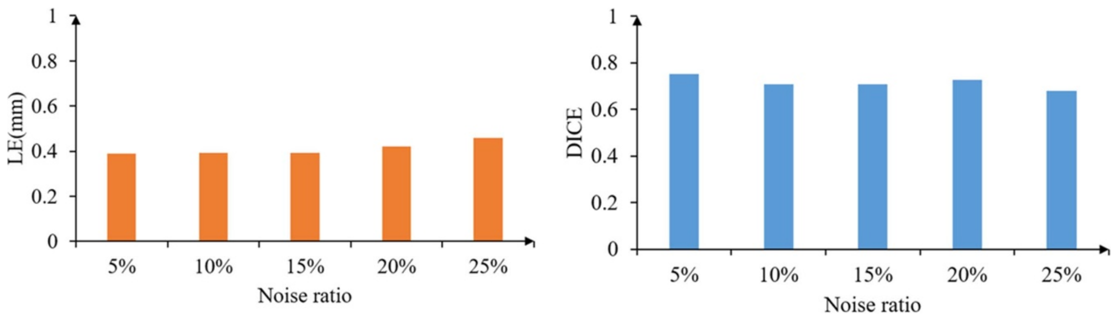

Figure 4. The Results of anti-noise experiments.

3.3. *In vivo* experiment and result

To further verify the effectiveness of our proposed method, in vivo mouse experiment was performed. The experiment followed strict guidelines and approval of the Animal Ethics Committee of Northwestern China University. Specifically, a 6-week-old adult BALB/C mouse was anesthetized during the experiment and we implanted a transparent glass tube (1 mm in diameter) filled with $Gd_2O_2S:Eu^{3+}$ NPs to simulate the early tumor. The coordinates of the implanted ball were (14.50, 9.50, 13.60) mm. The imaging system used in the experiment is designed as shown in figure 5. The system consists of a cone beam x-ray source (L9181-02,

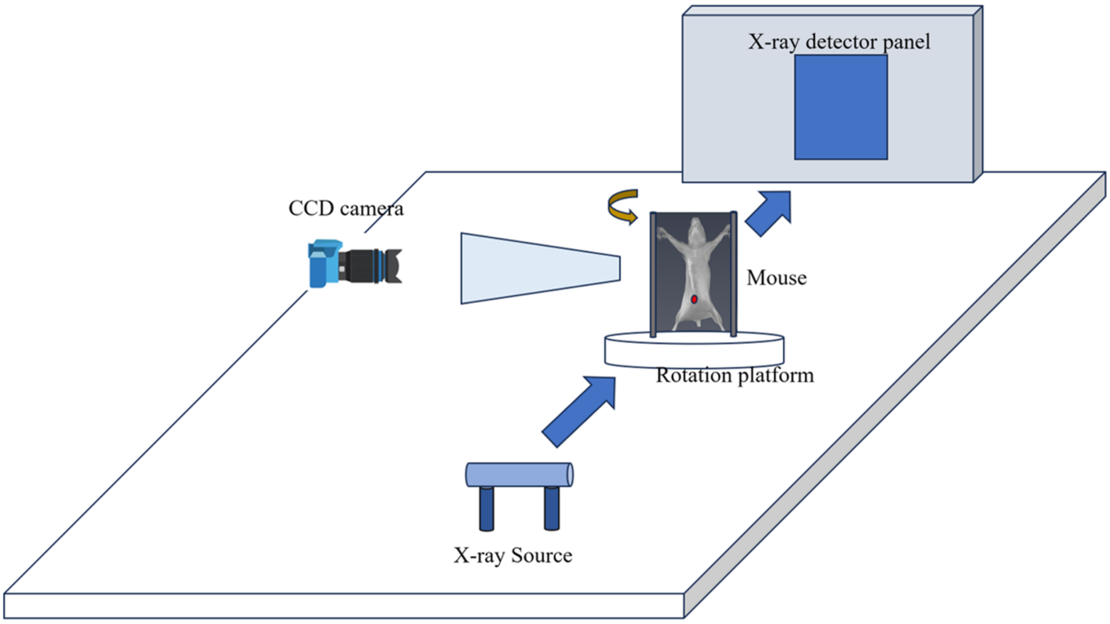

Figure 5. The imaging system used in the in vivo experiment.

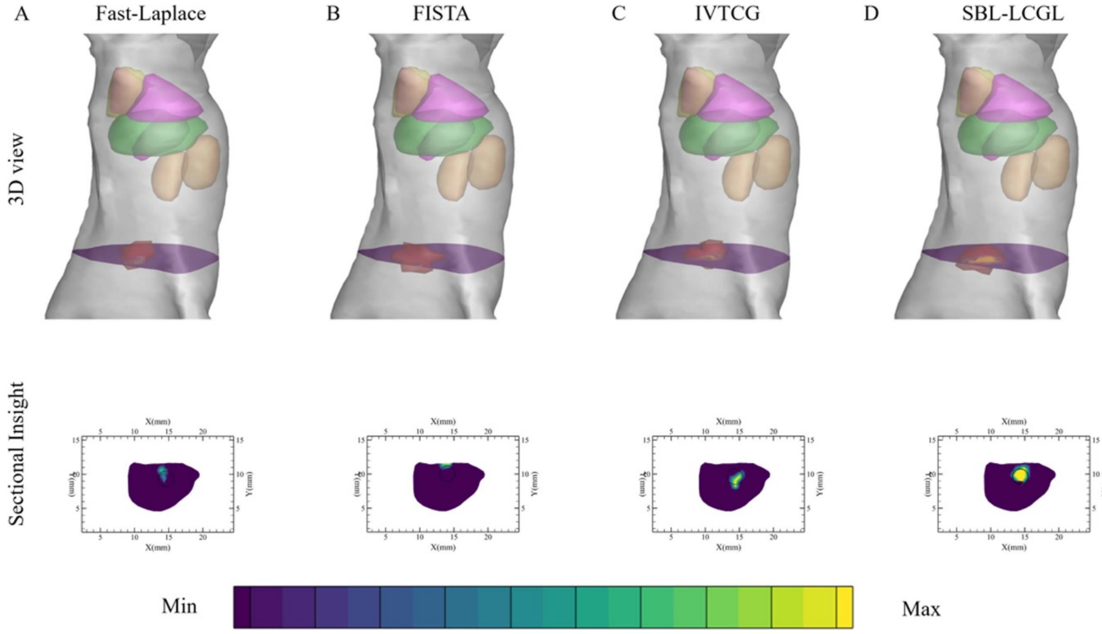

Figure 6. Reconstruction results of the in vivo experiment.

Hamamatsu Photonics, Hamamatsu, Japan), an x-ray detector panel (C7921CA-02, Hamamatsu, Japan), a CCD camera (iXon Ultra DU-897; Andor, UK), and a rotation platform. In detail, the voltage and current of the cone beam x-ray source were set to 48kV and 0.8 mA, respectively. The x-ray detector panel is used to detect x-ray transmitted through the mouse to generate high-resolution computed tomography (CT) images. In addition, we use the CCD camera to collect optical data at a wavelength of 650 nm. The exposure time and binning of CCD were set to 2 s and 1 × 1, respectively. In the course of the experiment, the mouse was rotated 1°each time by the turntable to obtain the corresponding CT images and x-ray projection data, thus ensuring the comprehensiveness and precision of the imaging data.

The results of the in vivo reconstruction are shown in figure 6, which shows a three-dimensional view and a two-dimensional cross-sectional view of the $z = 13.60\,\text{mm}$. The results of quantitative analysis are shown in table 4, from which it can be seen that the LE coefficient of the SBL-LCGL method is 0.4 mm, which is equal to half of the reconstruction error of the IVTCG and Fast-Laplace methods, indicating that

Table 4. Quantitative results in the in vivo experiment.

Method	True center position	Reconstructed center position	LE(mm)	DICE	MSE	SSIM	VR
Fast-Laplace	(14.50, 9.50, 13.60)	(14.13, 9.35, 14.36)	0.86	0.36	0.00389	0.809	1.39
FISTA	(14.50, 9.50, 13.60)	(13.89, 11.32, 14.38)	2.07	0.05	0.00973	0.793	1.12
IVTCG	(14.50, 9.50, 13.60)	(14.40, 8.92, 14.02)	0.71	0.46	0.00296	0.837	0.91
SBL-LCGL	(14.50, 9.50, 13.60)	(14.40, 9.89, 13.59)	0.40	0.75	0.00167	0.859	0.81

this method has great advantages in reconstruction accuracy. At the same time, the DICE coefficient reaches 0.75, which is also better than the other three methods. The MSE coefficient is 0.00167 and the SSIM is 0.859, which also confirms that the proposed method is superior to other methods. The VR coefficient of the IVTCG method is 0.91, but the VR coefficient of our method can also reach 0.81. There is not much difference. At the same time, in vivo experiments show that the performance of FISTA algorithm is not as good as that in the simulation of single light source experiments, which further confirms the limitations of FISTA algorithm in terms of robustness. It is proved that the proposed method is also very effective in living biological imaging, with high precision reconstruction accuracy and accurate morphological recovery ability.

4. Discussion and conclusion

CB-XLCT is an efficient hybrid optical molecular imaging technology that reconstructs the distribution of NPs sources in the body based on the light flux on biological surfaces. However, the reconstruction problem is essentially an inverse problem with ill-posedness, which will lead to low quality of the reconstructed image. We proposed an algorithm based on the sparse Bayesian framework to overcome the ill-posedness of the reconstruction problem. In the algorithm, the Laplace distribution is given as prior information on the light source distribution, and the hierarchical model is used to solve the problem of non-conjugation. This effectively combines sparsity and improves the accuracy of reconstruction. At the same time, the Lipschitz continuous gradient condition is used to replace the quadratic term of the likelihood function, and the conventional matrix inversion is transformed into a diagonal matrix inversion, thereby reducing the complexity of the algorithm. The expansion of the first-order Taylor formula for updating the loss function of hyperparameters leads to a convex problem that is easy to solve and improves the stability of the algorithm.

To evaluate the performance of the proposed method, three simulation experiments and one *in vivo* experiment were conducted, and the results were compared with those of three methods: Fast-Laplace, FISTA, and IVTCG. In single-light and dual-light experiments, the SBL-LCGL method has the lowest LE coefficient, the highest DICE coefficient, and the VR coefficient closest to 1. This shows that the proposed method has good reconstruction accuracy and shape recovery capabilities. In the anti-noise experiment, 5%, 10%, 15%, 20% and 25% Gaussian noise were added, respectively. The indicators obtained show that the method has strong robustness. In addition, *in vivo* experiments also confirmed the advantages in various indicators and verified the effectiveness of our proposed method in in vivo bioimaging.

However, there may be some possible limitations in this study. First, when the CCD camera collects data, because of the large number of photons, the noise is modeled as Gaussian noise, then in the case of a small number of photons, the modeling method of noise is not suitable, Poisson noise model can be used. Second, in deriving the posterior probability, in order to satisfy the simplicity of derivation, we propose some constraints, although these constraints are confirmed. Finally, there may be some differences in the optical properties of the reconstructed light source and the real light source and high-quality segmented images will also improve the reconstruction accuracy of CB-XLCT. Therefore, our future work can consider structural prior information and allow source area prior information, and analyze the impact of differences in optical properties on reconstruction quality.

In summary, a method based on SBL framework is proposed to improve the reconstruction quality of CB-XLCT. This method combines the sparsity of the NPs distribution and avoids complex matrix inversion. Through a series of simulations and *in vivo* experiment, it is confirmed that this method is superior to other typical methods in terms of reconstruction accuracy and shape recovery. We believe that the proposed method will help improve the quality of CB-XLCT reconstruction and expand its clinical application.

Data availability statement

The data cannot be made publicly available upon publication because no suitable repository exists for hosting data in this field of study. The data that support the findings of this study are available upon reasonable request from the authors.

Acknowledgments

This work was supported in part by the National Major Scientific Research Instrument Development Projects of China (82127805), in part by the Key Research and Development Program of Shaanxi Province (2024SF-YBXM-681, 2019GY215, 2021ZDLSF06-04), in part by the National Natural Science Foundation of China (61701403,61806164).

ORCID iDs

Yifan Wang https://orcid.org/0009-0001-7966-9801
Yi Chen https://orcid.org/0009-0006-4935-3546
Xin Cao https://orcid.org/0000-0003-3560-6523

References

Ahmad M, Pratx G, Bazalova M and Xing L 2014 X-ray luminescence and x-ray fluorescence computed tomography: new molecular imaging modalities *IEEE Access* **2** 1051–61

Bai Z 2023 Sparse Bayesian learning for sparse signal recovery using ℓ1/2-norm *Appl. Acoust.* **207** 109340

Bai Z, Shi L, Sun J and Christensen M G 2022 Space alternating variational estimation based sparse Bayesian learning for complex-value sparse signal recovery using adaptive Laplace priors *IET Signal Process.* **17**

Bai Z and Sun J 2023 Sparse Bayesian learning with automatic-weighting Laplace priors for sparse signal recovery *Comput. Stat.* **38** 2053–74

Chen D, Zhu S, Cao X, Zhao F and Liang J 2015 X-ray luminescence computed tomography imaging based on x-ray distribution model and adaptively split Bregman method *Biomed. Opt. Express* **6** 2649–63

Chen Y, Du M, Zhang G, Zhang J, Li K, Su L, Zhao F, Yi H and Cao X 2023 Sparse reconstruction based on dictionary learning and group structure strategy for cone-beam x-ray luminescence computed tomography *Opt. Express* **31** 24845–61

Ding X, Wang K, Jie B, Luo Y, Hu Z and Tian J 2014 Probability method for Cerenkov luminescence tomography based on conformance error minimization *Biomed. Opt. Express* **5** 2091–112

Fang J, Zhang L and Li H 2016 Two-dimensional pattern-coupled sparse bayesian learning via generalized approximate message passing *IEEE Trans. Image Process.* **25** 2920–30

Gao P, Cheng K, Schuler E, Jia M, Zhao W and Xing L 2020 Restarted primal-dual Newton conjugate gradient method for enhanced spatial resolution of reconstructed cone-beam x-ray luminescence computed tomography images *Phys. Med. Biol.* **65** 135008

Gao P, Rong J, Pu H, Liu T, Zhang W, Zhang X and Lu H 2018 Sparse view cone beam x-ray luminescence tomography based on truncated singular value decomposition *Opt. Express* **26** 23233–50

Glaubitz J 2023 Generalized sparse Bayesian learning and application to image reconstruction (https://doi.org/10.1137/22M147236X)

Guo H, Hu Z, He X, Zhang X, Liu M, Zhang Z, Shi X, Zheng S and Tian J 2017 Non-convex sparse regularization approach framework for high multiple-source resolution in Cerenkov luminescence tomography *Opt. Express* **25** 28068

Guo H, Yu J, Hu Z, Yi H, Hou Y and He X 2018 A hybrid clustering algorithm for multiple-source resolving in bioluminescence tomography *J. Biophoton.* **11** e201700056

Hu Z, Chen X, Liang J, Qu X, Chen D, Yang W, Wang J, Cao F and Tian J 2012 Single photon emission computed tomography-guided Cerenkov luminescence tomography *J. Appl. Phys.* **112** 024703

Jacques S L 2013 Corrigendum: optical properties of biological tissues: a review *Phys. Med. Biol.* **58** 5007–8

Kinsella J M, Jimenez R E, Karmali P P, Rush A M, Kotamraju V R, Gianneschi N C, Ruoslahti E, Stupack D and Sailor M J 2011 X-ray computed tomography imaging of breast cancer by using targeted peptide-labeled bismuth sulfide nanoparticles *Angew. Chem., Int. Ed.* **50** 12308–11

Klose A D, Beattie B J, Dehghani H, Vider L, Le C, Ponomarev V and Blasberg R 2010 In vivo bioluminescence tomography with a blocking-off finite-difference SP3 method and MRI/CT coregistration *Med. Phys.* **37** 329–38

Liu H, Yang X, Song T, Bao C, Shi L, Hu Z, Wang K and Tian J 2015 Multispectral hybrid Cerenkov luminescence tomography based on the finite element SPn method *J. Biomed. Opt.* **20** 86007

Liu T, Rong J, Gao P, Pu H, Zhang W, Zhang X, Liang Z and Lu H 2019 Regularized reconstruction based on joint L_1 and total variation for sparse-view cone-beam x-ray luminescence computed tomography *Biomed. Opt. Express* **10** 1–17

Liu T, Rong J, Gao P, Zhang W, Liu W, Zhang Y and Lu H 2018 Cone-beam x-ray luminescence computed tomography based on x-ray absorption dosage *J. Biomed. Opt.* **23** 1–11

Liu X, Ma S, Zhong S, Su A, Huang Z and Yi H 2021 Permissible region extraction strategies for XLCT: a comparative study *J. Phys.: Conf. Ser.* **2112**

Mishra S and Kappiyoor R 2014 Collimator width optimization in x-ray luminescent computed tomography (XLCT) with selective excitation scheme *J. Med. Imaging Health Inform.* **4** 641–86

Nesterov Y 2013 *Introductory Lectures on Convex Optimization: A Basic Course* vol 87 (Springer)

Oh M H, Lee N, Kim H, Park S P, Piao Y, Lee J, Jun S W, Moon W K, Choi S H and Hyeon T 2011 Large-scale synthesis of bioinert tantalum oxide nanoparticles for x-ray computed tomography imaging and bimodal image-guided sentinel lymph node mapping *J. Am. Chem. Soc.* **133** 5508–15

Parikh N 2014 Proximal algorithms *Found. Trends Optim.* **1** 127–239

Parvitte B, Risser C, Vallon R and Zéninari V 2013 Quantitative simulation of photoacoustic signals using finite element modelling software *Appl. Phys.* B **111** 383–9

Pratx G, Carpenter C M, Sun C, Rao R P and Xing L 2010 Tomographic molecular imaging of x-ray-excitable nanoparticles *Opt. Lett.* **35** 3345–7

Qin C, Zhong J, Hu Z, Yang X and Tian J 2011 Recent advances in Cerenkov luminescence and tomography imaging *IEEE J. Sel. Top. Quantum Electron.* **18** 1084–93

Ren S, Chen X, Wang H, Qu X, Wang G, Liang J and Tian J 2013 Molecular optical simulation environment (MOSE): a platform for the simulation of light propagation in turbid media *PLoS One* **8** e61304

Ruan C, Zhang Z, Jiang H, Dang J, Wu L and Zhang H 2023 Vector approximate message passing with sparse Bayesian learning for Gaussian mixture prior *China Commun.* **20** 57–69

Shutin D, Buchgraber T, Kulkarni S R and Poor H V 2011 Fast variational sparse bayesian learning with automatic relevance determination for superimposed signals *IEEE Trans. Signal Process.* **59** 6257–61

Sun Y, Babu P and Palomar D P 2017 Majorization-minimization algorithms in signal processing, communications, and machine learning *IEEE Trans. Signal Process.* **65** 794–816

Tang R, Zhang Q, Zhang W and Ma H 2022 Sparse Bayesian multiple sources localization using variational approximation for Laplace priors *Digit. Signal Process.* **126** 103460

Wang G, Cong W, Durairaj K, Qian X, Shen H, Sinn P, Hoffman E, McLennan G and Henry M 2006 *In vivo* mouse studies with bioluminescence tomography *Opt. Express* **14** 7801–9

Wu Y, Chen B, Liu K, Huang S, Li Y, Jia J and Yao J 2023 Bayesian image reconstruction using weighted laplace prior for lung respiratory monitoring with electrical impedance tomography *IEEE Trans. Instrum. Meas.* **72** 1–11

Yin L, Wang K, Tong T, Wang Q, An Y, Yang X and Tian J 2021 Adaptive grouping block sparse bayesian learning method for accurate and robust reconstruction in bioluminescence tomography *IEEE Trans. Biomed. Eng.* **68** 3388–98

Zhang G, Tzoumas S, Cheng K, Liu F, Liu J, Luo J, Bai J and Xing L 2018 Generalized adaptive gaussian markov random field for x-ray luminescence computed tomography *IEEE Trans. Biomed. Eng.* **65** 2130–3

Zhang L and Dai L 2022 Image reconstruction of electrical capacitance tomography based on an efficient sparse bayesian learning algorithm *IEEE Trans. Instrum. Meas.* **71** 1–14

Zhang Q, Zhao H, Chen D, Qu X, Chen X, He X, Li W, Hu Z, Liu J and Liang J 2011 Source sparsity based primal-dual interior-point method for three-dimensional bioluminescence tomography *Opt. Commun.* **284** 5871–6

Zhang S, Liu Y, Li X and Bi G 2017 Variational bayesian sparse signal recovery with LSM prior *IEEE Access* **5** 26690–702

Zhang Y, Lun M C, Li C and Zhou Z 2019 Method for improving the spatial resolution of narrow x-ray beam-based x-ray luminescence computed tomography imaging *J. Biomed. Opt.* **24** 1–11

Zhao J, Guo H, Yu J, Yi H, Hou Y and He X 2021 A robust elastic net-$l_1l_2$reconstruction method for x-ray luminescence computed tomography *Phys. Med. Biol.* **66** 195005